ARTICLE

# Shape Transformation Mechanism of Gold Nanoplates

Back Kyu Choi, Jeongwon Kim, Zhen Luo, Joodeok Kim, Jeong Hyun Kim, Taeghwan Hyeon,* Shafigh Mehraeen,* Sungho Park,* and Jungwon Park*

ACCESS | Metrics & More | Article Recommendations | Supporting Information

**ABSTRACT:** Shape control is of key importance in utilizing the structure–property relationship of nanocrystals. The high surface-to-volume ratio of nanocrystals induces dynamic surface reactions on exposed facets of nanocrystals, such as adsorption, desorption, and diffusion of surface atoms, all of which are important in overall shape transformation. However, it is difficult to track shape transformation of nanocrystals and understand the underlying mechanism at the level of distinguishing events on individual facets. Herein, we investigate changes of individual surface-exposed facets during diverse shape transformations of Au nanocrystals using liquid phase TEM in various chemical potentials and kinetic Monte Carlo simulations. The results reveal that the diffusion of surface atoms on nanocrystals is the governing factor in determining the final structure in shape transformation, causing the fast transformation of unstable facets to truncated morphology with minimized surface energy. The role of surface diffusion introduced here can be further applied to understanding the formation mechanism of variously shaped nanocrystals.

**KEYWORDS:** liquid phase TEM, gold nanoplate, shape transformation, surface structure, surface diffusion
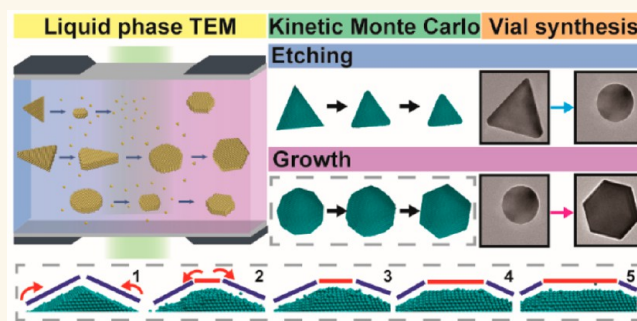
Shape control is primarily important in the synthesis of nanocrystals since they have a strong structure–property relationship.[1−3] Nanocrystals have a high surface-to-volume ratio, inherently making them prone to diverse structure transformations.[4,5] The structure transformation dynamically occurs during the synthesis of nanocrystals for the formation of the desired morphology.[6−8] Synthesized nanocrystals are not always static and undergo further transitions with respect to morphology and composition.[9−12] For nanocrystals of a few nanometers in size, the crystallographic facets of exposed surfaces are not easily identified.[13] In this case, chemical potential difference between surface-exposed atoms and monomers in the solution, regulated by the concentration of monomers and the type of ligands, controls the rates of adsorption and desorption reactions occurring on the nanocrystal surface.[4,14] The ratio of adsorption to desorption determines the direction of the transformation, either toward the growth or etching of the nanocrystals. As the nanocrystals grow, they develop distinctly faceted morphology according to its own crystal structure. Because each surface-exposed facet has different surface free energy, the chemical potential of monomers in a solution inconsistently competes with the one of surface atoms on different facets.[15] Consequently, monomers in the solution

prefer to attach to the relatively unstable facets, driving directional growth toward the formation of anisotropic nanocrystal structure.[6] The synthesis of anisotropic or faceted nanocrystals can be realized by changing the reaction conditions during the colloidal synthesis of nanocrystals.[11,12,16,17]

Another important factor that contributes to the shape transformation of nanocrystals is the diffusion of surface atoms.[9] Depending on the type of materials and surface ligands, atoms on the nanocrystal surface may not stand still. They can move on the surface by overcoming the potential energy barrier of the diffusion, which is closely related to the surface structure and geometry.[18] In addition, in the nanoscale regime, the surface-to-volume ratio dramatically increases, and the surface structure of the nanocrystal itself becomes complicated. The diffusion coefficient of surface metal atoms,
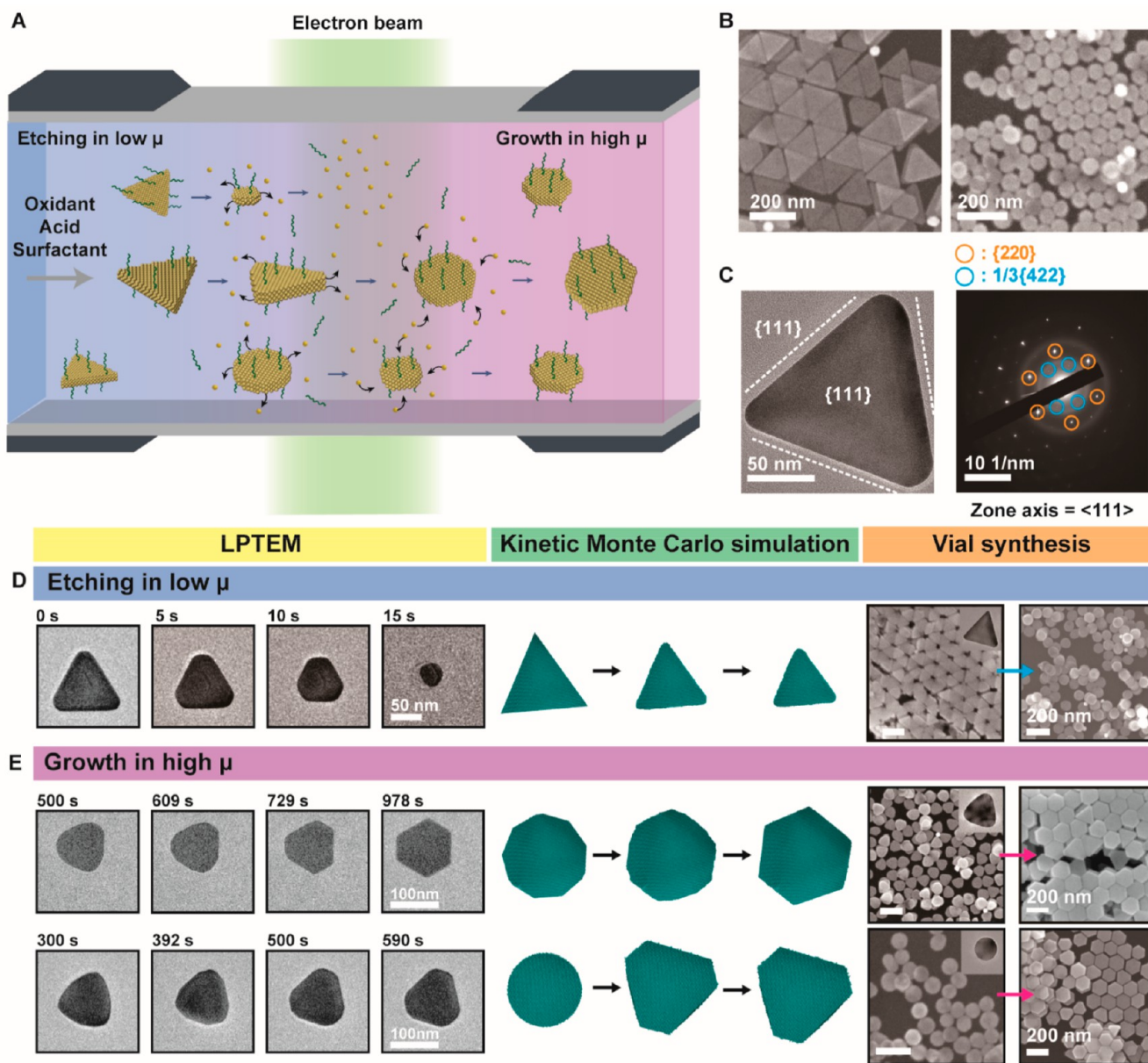
A

Figure 1. Overall experimental setup and diverse shape transformation of Au nanocrystal. (A) Schematic illustration of a LPTEM cell for observing diverse shape transformations of Au nanocrystals. (B) SEM images of synthesized Au nanoprisms and circular nanoplates. (C) TEM image of an Au nanoprism and the corresponding electron diffraction patterns. (D) Snapshots taken from LPTEM, KMC simulations, and vial synthesis, presenting the etching of Au nanoprisms in the oxidant solution, and (E) reformation of the etched Au nanoprisms of different initial configurations. KMC simulation snapshots are obtained at $t/t_0$ = 0, 200, and 400 time points. The chemical potentials are $\mu$ = −2.00 eV and $\mu$ = −1.75 eV in (D) and (E), respectively. In KMC simulations, bond energy and the diffusion energy barrier are held constant at $\varepsilon$ = 0.33 eV and $\varepsilon_{diff}$ = 0.1 eV, respectively.

which is in the range of 0.1−10 nm$^2$/s at room temperature,[19−21] implies that the surface diffusion, if activated, can significantly affect the overall shape transformations. The surface diffusion is presumably regulated by the surfactant incorporated in the colloidal nanocrystal syntheses.[22] In certain cases, surfactant molecules can selectively passivate specific facets of the nanocrystal, consequently changing the dynamics of the surface atom diffusion.[23−25] Thus, shape transformation of nanocrystals is to be interpreted as a consequence of the complex balance between adsorption, desorption, and diffusion of surface atoms, which varies on different surface-exposed facets of the nanocrystals. However, understanding the pathway and underlying mechanism of the shape trans-

formation of colloidal nanocrystals is a complex task due to the difficulty in probing the changes occurring on individual facets of the nanocrystals. Spectroscopic methods have been used, but they were only possible to track the transformation of nanocrystals that have a strict scaling relationship between their morphology and optical response.[26−28] In addition, they only provide averaged information on many nanocrystals in a solution and barely decipher important events occurring in the individual trajectories of the nanocrystal transformation.

Recently, liquid phase transmission electron microscopy (LPTEM) was developed and enabled real-time observation of individual nanocrystals dispersed in solution.[29−31] For example, growth to various shapes of nanoparticles and

dissolution of synthesized nanoparticles have been successfully tracked in real time by LPTEM.[32−37] These studies elucidated that controlling chemical conditions in the nanoparticle solution is important to control the shape of nanoparticles. It was also reported that, in single-nanoparticle trajectories, there are multiple different pathways involved for the formation of homogeneous nanoparticles.[38,39] Nonetheless, it has been challenging to differentiate structure changes on individual surface-exposed facets that occur as a result of the balance between important surface processes, such as monomer adsorption/desorption and surface diffusion, and how the structure changes respond to the chemical condition in solution while developing a specific morphology of nano-particles.

Herein, we use LPTEM to directly observe transitions of individual surface-exposed facets of Au nanocrystals during their diverse shape transformations, including the oxidative etching of Au nanoprisms and reformation of faceted structure at different monomer concentrations. In situ analysis combined with kinetic Monte Carlo (KMC) simulations elucidates that diffusion of surface atoms determines the final structure in Au nanocrystal transformation and is a key factor for the formation of truncated morphology with minimized surface energy.

## RESULTS AND DISCUSSION

**Oxidative Etching of Au Nanoprisms.** The overall design of the LPTEM experiment to investigate various shape transformations of Au nanoprism is introduced in Figure 1A. Au nanoprisms are synthesized by following a three-step seed-mediated method (Figure 1B).[40] Synthesized Au nanoprisms have homogeneous morphology with the basal plane composed of a {111} facet of face-centered cubic (FCC) crystal structure (Figure 1C and Figure S1). In the selected area electron diffraction (SAED) and fast Fourier transform (FFT) patterns, we find 1/3 {422} spots directing to the tip site of the nanoprism, which is commonly observed in Au nanoplates with stacking faults parallel to the basal {111} plane.[6,34,36,41−44] This stacking fault of the twin plane is known to generate convex {111} on the surface-exposed side facets of the Au nanoprism. To induce shape transformations of Au nanoprisms, a mixture of $H_2O_2$, HCl, and cetyltrimethylam-monium bromide (CTAB) is used as an etching solution. $H_2O_2$ oxidizes the Au atoms on the nanoprism surface, and HCl can facilitate the oxidative etching since the reduction potential of $AuCl_4^-$ ($AuCl_4^- + 3e^- \rightarrow Au(s) + 4Cl^-$, $E(V) = 1.00$ V), generated in the presence of HCl, is lower than that of $Au^{3+}$ ($Au^{3+} + 3e^- \rightarrow Au(s)$, $E(V) = 1.52$ V) or $Au^+$ ($Au^+ + e^- \rightarrow Au(s)$, $E(V) = 1.83$ V).[45,46] CTAB, which consists of $CTA^+$ and $Br^-$, generates cationic micelles around the Au nanocrystal surface and acts as a surfactant along with a halide counterion during the reaction (Figure S2).[47,48] $Br^-$ in CTAB can also facilitate the oxidative etching of Au nanoprisms by generating $AuBr_4^-$ with low reduction potential and $Br_3^-$ oxidant in the presence of $H_2O_2$.[46,47] For LPTEM observation of shape transformations, a solution of Au nanoprisms is loaded in the liquid cell and the etchant solution is subsequently injected into the liquid cell through the syringe pump (Figure 1A). In parallel, the same reaction is also conducted by loading the $H_2O_2$, HCl, and CTAB into the vial of Au nanoprism solution. With a sufficient oxidizing strength of the etching solution, Au atoms on the surface of the Au nanoprism can be oxidized to $AuCl_4^-$, dissolving out into the solution (Figure 1A,D, Figures S3−S5, and Videos S1 and S2).[49,50] While oxidative etching

occurs, the surfactant, CTAB, can passivate the flat surfaces of Au nanoprism, facilitating the access of oxidants to curved surfaces.[48,51] During the etching, Br anions can adsorb on Au surfaces, which induces partial charge transfer and decreases activation entropy for surface diffusion process.[52,53] As a result, the surface diffusion of atomic Au is promoted and the regions with high curvature is smoothened.[53−56] Thus, Au atoms on the tip sites of the Au nanoprism are etched out first, generating a circular nanoplate, as indicated by the increase of circularity during the dissolution (Figure 1D and Figure S5). The shape transformation from Au nanoprism to circular nanoplate is consistently observed in LPTEM and the vial reaction (Figures S6 and S7).

To understand the mechanism of the nanocrystal shape transformation in the presence of a surfactant, we perform a series of computer simulations. For these simulations, we utilize the lattice gas KMC method.[57] We particularly focus on the shape transformation process on an fcc lattice such as Au nanocrystal growth studied in this work. Our model only resolves the lattice sites that are occupied by Au atoms or vacant. The reaction rates change on lattice sites as a result of stochastic events, which include (1) adsorption onto a vacant lattice site, (2) desorption from an occupied lattice site, and (3) diffusion to one of the 12 near neighbors for an fcc lattice site (see Supporting Information for more details). According to the KMC model, when the ratio of the chemical potential to the bond energy, $\mu/\varepsilon < -6$, the shape transformation is dominated by etching of the nanocrystal.[32] As shown in Figure 1D, KMC simulation results exhibit a competition between atom desorption and surface diffusion. Since the tip sites have lower coordination number compared to the flat surfaces, Au atoms on the tip sites tend to dissociate, which facilitates the etching process and results in the decrease of the nanocrystal size with rounding of the corners. It is noteworthy that the nanocrystal configurations during etching obtained from the KMC simulation results are in reasonable agreement with those from the LPTEM, and vial reaction (Figure 1D and Figure S6).

**Reformation of a Faceted Structure.** As the chemical etching proceeds in the entire liquid cell, dissolved Au ions are continuously accumulated in the solution. The accumulated Au ions can facilitate adsorption of monomers back onto the surface of the etched nanocrystal, while the irradiated electron beam serves as a reductive environment.[39,58] The monomer concentration in the solution, which is directly correlated with the chemical potential, increases during the etching process. As a result, the etching gradually slows down and adsorption of Au atoms onto the surface of the nanocrystal dominates the overall reaction, eventually inducing reformation of Au circular nanoplates (Figure 1A and Videos S3 and S4). Overall, starting from a nanoprism, the nanocrystal shrinks to a circular nanoplate and then regrows to have a hexagonal plate morphology (Figure 1E). Interestingly, although the shapes of the etched nanoprisms are not homogeneous at the start of growth, possibly due to the heterogeneous local environment in the LPTEM, they all evolve into the uniform hexagonal nanoplates after the reformation. These results indicate that there is another important factor, besides the initial shape and local environment in the solution, that actually drives the nanocrystal shape transformation and dominates in determin-ing the final structure of the growth product, which will be discussed below.
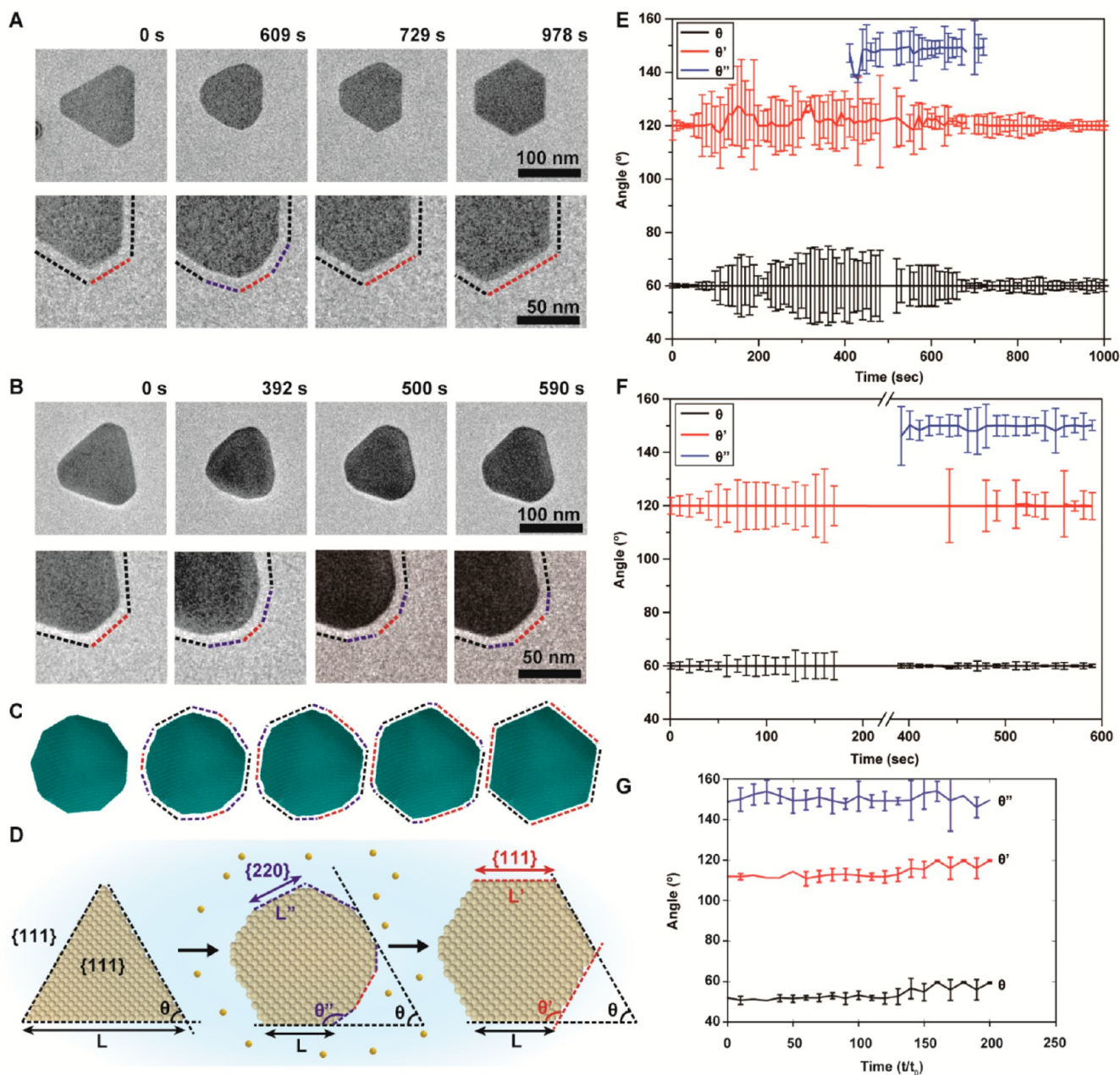
Figure 2. Reformation of faceted structure to the Au hexagonal nanoplate. (A,B) TEM snapshots (top) and magnified TEM images (bottom) of Au nanocrystal etching, followed by reformation. The colored dashed lines in the bottom row presents the three distinct surface-exposed side facets during the shape transformation, matching with those in (C,D). (C) Snapshots from KMC simulations at $t/t_0 = 0$, 100, 200, 300, and 400 time points, illustrating the progression of growth of a 9-membered ring polygonal nanocrystal to a hexagonal configuration. The chemical potential, bond energy, and diffusion energy barrier are $\mu = -1.75$ eV, $\varepsilon = 0.33$ eV, and $\varepsilon_{diff} = 0.1$ eV, respectively. (D) Illustration of side facet analysis. (E,F) Time-series analysis of angle between a pair of side facets shown in (A,B), averaged over the angles of the same type in (D). (G) Time-series analysis of angles between a pair of side edges shown in (C), averaged over 5 simulations.

Before the sequential reformation starts to occur, the Au nanoprism is observed to be etched out into a rounded shape (Figure S8). We note that the surfactants also passivate the flat surfaces of the Au nanoprism, and atoms on the tip sites dissolve into the solution, resulting in the etching preferentially from the tip site.[48,51] After the reformation caused by the increased chemical potential, contrast intensity of the hexagonal plates almost stays the same compared to the initial Au nanoprisms (Figure S8). It indicates that the surfactants continuously passivate the basal plane during the entire reaction, inducing two-dimensional growth only on the side

directions (Figures S2 and S9).[59] In addition, while sequential reformation occurs after the nanoprism etching, we are able to observe the development and disappearance of intermediate facets, leading to the hexagonal plate morphology (Figure 2A,B). Also from the KMC simulation results, when the ratio of the chemical potential to the bond energy, $\mu/\varepsilon \geq -6$, we observe the same growth process starting from the polygonal nanocrystal to a hexagonal configuration, along with the disappearance of the intermediate facets (Figure 2C and Figure S10). This growth aspect observed in both LPTEM and KMC
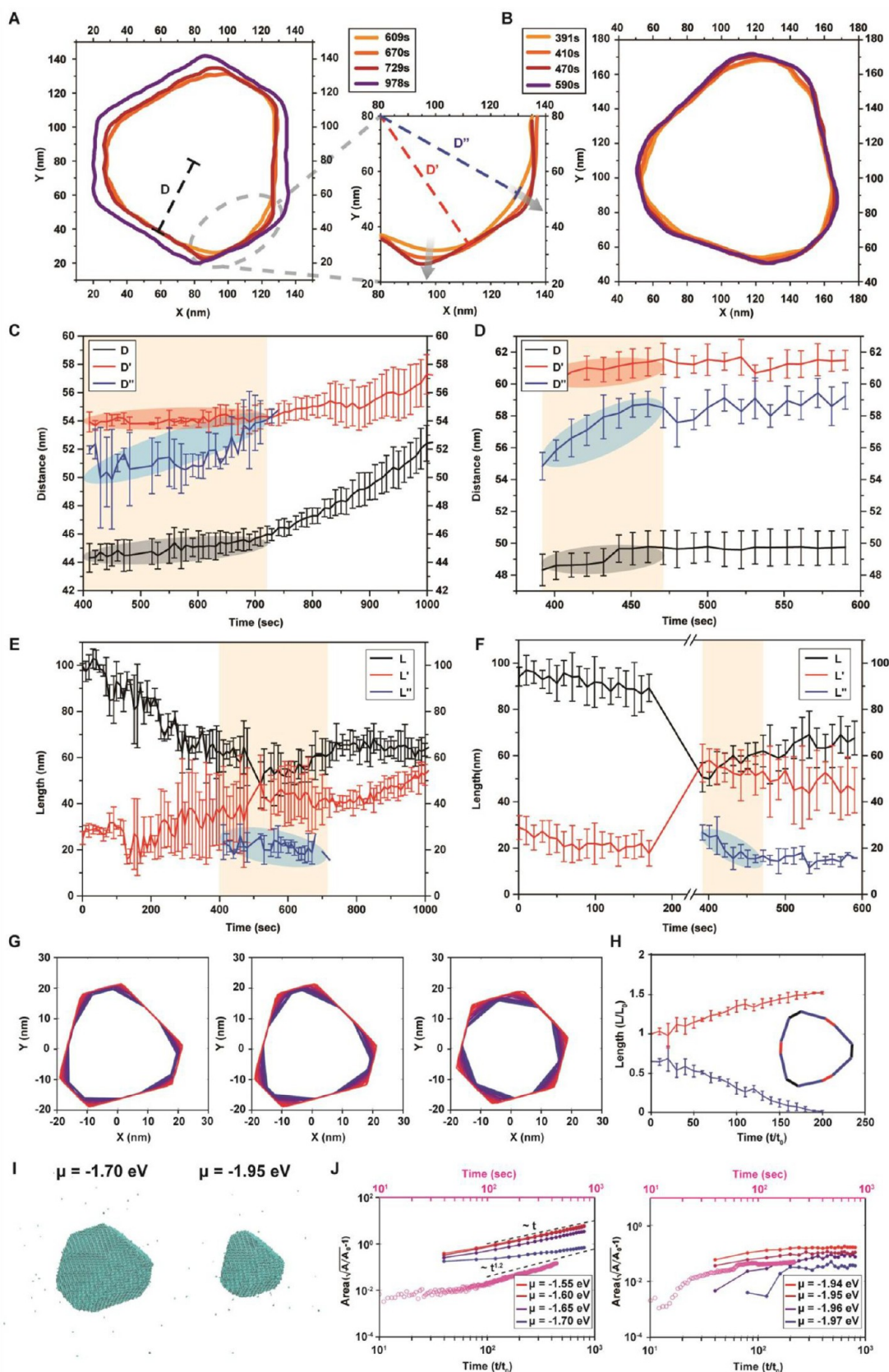
**Figure 3. Analysis of surface-exposed facet development from individual side facets. (A,B) Reformation trajectories of two etched Au nanoprisms, (C,D) time-series analysis of the distance between the center of mass of the projected area onto {111} basal plane and each side facet and (E,F) time-series analysis of length of side facets shown in Figure 2A,B. The shaded area in (C−F) indicates the initial period of reformation where the intermediate {220} facets are rapidly transformed to {111} facets. (G) Reformation trajectories obtained from KMC simulations, where 12- and 9-membered ring polygonal nanocrystals with different initial configuration grow into a hexagonal configuration,**

Figure 3. continued

from blue to red. (H) Time-series analysis of nondimensional length of side facets for the initial 9-membered ring polygonal nanocrystal shown in (G) (right panel), averaged over 5 simulations. In these simulations, the chemical potential, bond energy, and diffusion energetic barrier are $\mu = -1.75$ eV, $\varepsilon = 0.33$ eV, and $\varepsilon_{diff} = 0.1$ eV, respectively. (I) Snapshots from KMC simulations, obtained at $t/t_0 = 400$ time point for high chemical potential (left) and the chemical potential slightly above the etching regime (right), while $\varepsilon = 0.33$ eV, and $\varepsilon_{diff} = 0.1$ eV are held constant. (J) Time-series analysis of the projected area onto {111} basal plane of nanocrystals for high chemical potential (left) and the chemical potential slightly above the etching regime (right). KMC simulations are represented by solid lines and LPTEM results are represented by pink open circles.

simulations at high chemical potential regime is reproduced in vial synthesis as shown in Figure 1E and Figure S11.

**Evolution of Individual Facets in the Formation of Au Hexagonal Nanoplates.** We split in situ TEM movies into time-series snapshot images, binarize them to black and white images, and extract morphological information such as length and adjoining angle of surface-exposed side facets using a homemade Matlab algorithm (Figure 2D). This technique provides in situ information to investigate the detailed shape transformation of Au nanocrystals at the individual facet level. Using the known crystal structure of the initial Au nanoprism and Miller indices of its surface-exposed facets, we can define the Miller indices of facets evolving during the shape transformations (Figure 2A,B) by measuring the internal angle between the evolving facets and the initial side facet of the nanoprism (marked with black L in Figure 2D). The angle between initial side facets of the nanoprism ($\theta$) is 60° (Figure 2E,F), and the direction to each projected edge from the nanoprism center is $\langle 422 \rangle$, which can be derived from the direction to the 1/3 {422} spots from the center of SAED and FFT patterns (Figure 1C and Figure S1). In the reformation after oxidative etching, new facets (marked with red L′ in Figure 2D) appear and grow to form the hexagonal plate morphology. The angle between L and L′ ($\theta′$) is maintained at approximately 120° (Figure 2E,F), indicating that the direction to L′ from the nanoplate center is also $\langle 422 \rangle$. It is well-known that Au hexagonal nanoplates with $\langle 422 \rangle$ directions perpendicular to the projected edges have convex or concave {111} as surface-exposed facets on the side planes.[6,34,36,41−44] The hexagonal nanoplates obtained from the reformation are likely to follow the same crystal structure (Figure 2A,B). In addition, there is another family of facets that evolves temporarily and disappears (marked with blue L″ in Figure 2D) during the reformation. They turn out to have an internal angle ($\theta″$) of ~150° with the projected edges of the initial nanoprism (the angle between black and blue dotted lines in Figure 2A,B), as shown in Figure 2E,F. The direction which makes a 150° angle with $\langle 422 \rangle$ corresponds to $\langle 220 \rangle$, indicating that the {220} facets are exposed as the intermediate side facets during the reformation. Those three distinct angles, $\theta$, $\theta′$, and $\theta″$, are also analyzed in nanoparticle trajectories from KMC simulations (Figure 2C and Figure S10). To ensure that two stable angles, $\theta$ and $\theta′$, are 60 and 120°, respectively, at the long-time limit, we intentionally start the simulations with initial configuration whose angles are lower than and different from the stable angles (Figure 2G and Figure S10). If the dynamics of reformation is properly captured in KMC simulations, those angles should converge to the stable values same as LPTEM results, which also indicate the specific feature of these values. As shown in Figure 2G and Figure S10, KMC simulation results indicate that the angles converge to 60 and 120°, respectively, after ~200 time units and slightly fluctuate around these angles as the reformation proceeds. Overall,

Figure 2G and Figure S10 suggest consistency with LPTEM results. The black and red surface facets, corresponding to {111} facets, eventually constitute the hexagonal nanoplate, while {220} facets, indicated by the blue dotted lines, are temporarily exposed during the growth process. Furthermore, it is noteworthy that in all tracked surface-exposed side facets, measured angles between the side facets are invariant during the entire reaction, which indicates that the outward propagation of the exposed facets is maintained in the same direction with respect to the center of the nanoplate during the reformation.

**Growth Kinetics Observed at Individual Surface-Exposed Facets.** Shape transformation from the etched Au nanoprism to the hexagonal nanoplate under high chemical potential conditions can be deconvoluted into the growth rates of individual side facets. We track the distance between each projected edge and center of mass of the projected area using the growth trajectory, as shown in Figure 3A,B. Interestingly, during the initial period of reformation, the intermediate {220} facets quickly advance and eventually disappear, while {111} side facets stay stagnant, which induces the shape transformation of a polygonal nanocrystal into a hexagonal plate. This growth aspect is clearly evidenced by the morphology changes (Figure 3A,B), and the time trajectory of distances between the projected edges and the particle center of mass (Figure 3C,D). While the distance of {220} side facet (L″) from the center of mass of the projected area dominantly increases (marked as D″ in Figure 3C,D), the distance of initial {111} side facets L (marked as D) and side facets L′ (marked as D′) from the center of mass of the projected area, remains almost constant during the initial reformation. In addition, as the {220} facet is rapidly transformed to {111} facet, the length of L″ decreases while the length of L′ increases overall, which is shown in Figure 3E,F (see also Figure S12). These results imply that monomers in the solution are primarily consumed to transform {220} into {111} facets during the initial reformation. Consequently, the side facets L and L′ are only extended but do not advance (Figure 3C−F).

The dominant development of the intermediate facets is also prominent in the growth trajectories obtained from KMC simulations. Figure 3G illustrates the simulated progression of nanocrystal growth starting from different initial configurations of 12- and 9-sided polygons in the left two and right panels, respectively. Although the initial configurations are different, they all converge into a hexagonal configuration. A closer look at Figure 3G reveals that, during the growth process, the projected edges stay parallel to the initial edges, regardless of the initial edge angle. Figure 3G also indicates that the length of intermediate facets decreases as they move perpendicularly to the edge normal direction, whereas the length of stable facets increases before the shapes converge to a hexagonal configuration. The length of stable (red) and intermediate (blue) facets projected onto {111} basal plane, normalized by
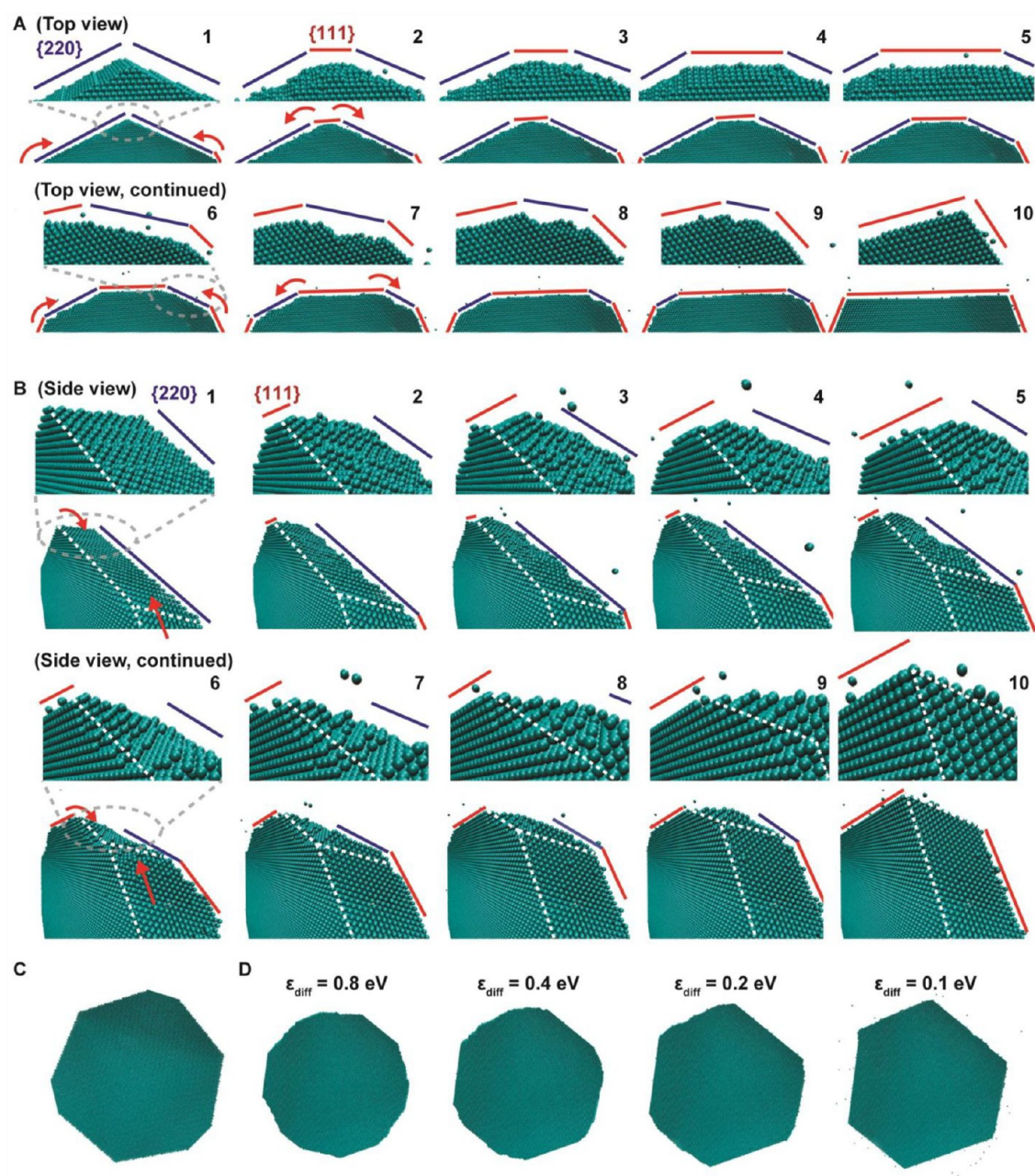
**Figure 4.** Reformation mechanism of Au nanocrystals from KMC simulations. Atomic-scale 3D view of the progression (left to right, top to bottom) of a Au nanocrystal growth from the (A) top view and (B) side view shown in Figure 2C. Edges of the stable facets are marked by red lines, and disappearing edges of the unstable facets are marked by blue lines. Top rows are the magnified images of the bottom rows, presenting the rough surface composed of kink and step sites on unstable facets, compared to the smooth stable facets. (C) Initial configuration of 9-membered ring polygonal nanocrystal and (D) corresponding final configurations at $t/t_0 = 400$ time point for different diffusion barrier, obtained from KMC simulations, where chemical potential and bond energy, $\mu = -1.75$ eV and $\varepsilon = 0.33$ eV, respectively, are held constant.

the initial length of the stable facet, is plotted against nondimensionalized time $(t/t_0)$ in Figure 3H. In this trajectory, $t_0$ is the reciprocal of the event rate constant in KMC simulations (see Supporting Information for more details). The results in Figure 3H also confirm our finding that the length of an intermediate side facet decreases and that of a stable side facet increases with time as the growth process continues until the intermediate side facet completely vanishes.

From the LPTEM experiments and KMC simulation results in high chemical potential regime, we note that the initial configurations of nanocrystals from the moment the reformation starts are heterogeneous. Nonetheless, they all converge to hexagonal nanoplates via the dominant development and transformation of the surface-exposed {220} facets. We also observe from Figure 3A that {111} facets start to advance and grow after the intermediate {220} facets completely vanish. Thus, the distances D and D′ start to increase after the dominant development of {220}, while the number of surface-exposed side facets decreases and the projected area continuously increases (Figure 3C and Figure

G

S12). However, in Figure 3B, additional growth of {111} side facets does not occur, even after the {220} facets stop advancing (Figure 3D and Figure S12). Additional growth of {111} side facets after the hexagonal nanoplate reformation can be deduced from the high concentration of Au monomers in the liquid solution, which is confirmed by the KMC simulations (Figure 3I and Figure S13). The increase of the Au monomer concentration, thereby increasing the chemical potential in the solution, can induce further growth of the hexagonal nanoplate, as illustrated in Figure 3I and Figure S13. After the intermediate facets disappear, layer-by-layer deposition can occur on surface-exposed {111} facets (Figure S14), which is manifested by the increase of D and D′ in Figure 3C. The trajectory of the projected area illustrates a continuous increase, which indicates a continuous growth of nanocrystal, shown in the left panel of Figure 3J and Figure S13. Figure 3J also compares the trajectories of the normalized projected area ($\sqrt{A/A_0} - 1$) at high chemical potential regime (left panel) and the chemical potential slightly above the etching regime (right panel), where $A_0$ is the initial projected area. The KMC simulation results in the left panel of Figure 3J suggest that the normalized projected area grows linearly with time, $\sim t$ (dashed lines), at high chemical potential, which is in reasonable agreement with the power law, $\sim t^{1.2}$, of the LPTEM result (pink open circles) taken from Figure 3A.[35,60] However, if the chemical potential is slightly above the etching regime ($\mu/\varepsilon \geq -6$ or $\mu \geq -1.98$ with $\varepsilon = 0.33$ eV), growth process is retarded, and additional growth does not occur after the unstable intermediate facets vanish. In this case, the normalized projected area of nanocrystals initially increases but nearly stops growing soon after, showing a sublinear growth overall (right panel of Figure 3J and Figure S13).

**Reformation Mechanism of Au Nanocrystal and the Effect of Surface Diffusion.** Although the Au monomers in the liquid solution can be adsorbed to {220} as well as {111} facets, only the surface-exposed {220} facets predominantly develop until they totally disappear. This mechanism can be deduced from the significant diffusion of Au atoms on the nanocrystal surface. This surface diffusion is verified when we look at the progression of nanocrystal reformation in high chemical potential regime from KMC simulations in atomic scale, as illustrated in Figure 4A,B. Since {220} facets are less closely packed than {111} facets, and thus have higher surface free energy in FCC crystal system,[61,62] they contain more dangling bonds, kinks, or step sites where the surface atoms can easily diffuse and occupy (Figure S15).[23] The surface diffusion is driven by surface-energy reduction, and leads to the reformation of nanocrystal surface.[63] As a result, when the Au monomers start to get adsorbed on the nanocrystal surface at high chemical potential regime, they quickly diffuse to unstable {220} facets, heavily contributing to layer-by-layer out-of-plane growth of {220}. On the {111} facets, however, only in-plane expansion is apparent until {220} fully develops and vanishes, eventually generating a nanoplate with hexagonal structure.

To demonstrate the effect of surface diffusion on the growth mechanism, we perform a series of KMC simulations with different energy barriers to the surface diffusion. To better understand the impact of surface diffusion on the final configuration of nanocrystal in the growth process, we start these simulations from the same initial configuration of the nanocrystal. Figure 4C shows the top view projected into {111} basal plane with 9-membered ring of the initial

configuration, and Figure 4D illustrates the snapshots of the nanocrystal configuration at $t/t_0 = 400$ time point for different values of the surface diffusion energetic barriers ($\varepsilon_{\text{diff}}$), taken from KMC simulations. When diffusion barrier is high ($\varepsilon_{\text{diff}} = 0.8$ eV, Figure 4D), surface atoms cannot readily diffuse to the unstable facets. Hence, the final configuration becomes similar to the initial configuration composed of unstable high-index rough facets as surface-exposed side facets. As the energy barrier decreases, diffusion to unstable facets is facilitated, generating a nanoplate of hexagonal configuration with stable {111} side facets ($\varepsilon_{\text{diff}} = 0.1$ eV, Figure 4D).

The importance of surface diffusion in determining the final nanocrystal structure is also confirmed by other LPTEM experiments, KMC simulations, and vial synthesis. We synthesize Au circular nanoplate as a starting material in LPTEM experiment, and inject the same etchant solution into the liquid cell, as illustrated in Figure 1B and Figure S16. Consequently, the etching followed by sequential reformation and growth is reproduced for Au circular nanoplate as well, and the final product is also hexagonal plate truncated with stable {111} facets (Figure S17 and Video S5). In KMC simulations, we look at the progression of the growth starting from circular nanoplate and prism nanocrystals, all of which conclusively indicate that the final structure is a hexagonal plate (Figure S18). It is noteworthy that the intermediate configurations look different for different initial shapes, and are dependent on the initial configurations. However, the long-time observations, during which surface diffusion is actively affecting the growth process, suggest an ultimate hexagonal plate and independence of the initial configuration.

In a control experiment, we inject a mixture of $H_2O_2$, HCl, and cetyltrimethylammonium chloride (CTAC) into the liquid cell instead of CTAB. It is known that the affinity of Cl⁻ with Au metal surface is lower than that of Br⁻, so are the surface density of Cl⁻ and counterion CTA⁺ on Au nanocrystal surfaces.[25,59,64] It results in the reduction of surface passivation and promotion of the adsorption/desorption of surface Au atoms when CTAB is replaced by CTAC. It possibly weakens the contribution of surface atom diffusion to the shape transformation. The etching followed by sequential reformation and growth is reproduced in a control experiment with CTAC, as shown in Figure S19 and Videos S6 and S7. However, there are differences in the case of CTAC. The etched nanoprisms do not always grow to hexagonal nanoplate. Deposition of Au atoms on the basal plane for the formation of 3D morphology also frequently occurs (Figure S19). Reduced surface passivation by CTAC makes etched nanoprism highly affected by the local environment, inducing the heterogeneity in the degree of etching and the pathway of the regrowth. Consequently, it reveals that suppressing the surface diffusion can disturb the homogeneous fine control of shape evolution, implying that controlling the surface diffusion, with respect to the degree of the surface reaction such as monomer adsorption and desorption, can be an important direction to induce the homogeneous shape of the nanocrystals truncated with stable low-index facets.

In the vial synthesis, we use nanoprisms with sharp corners and round corners as the starting materials for the growth reaction, and all the final structures turn out to be hexagonal nanoplates as shown in Figure S20. Plasmon peaks of starting materials from the extinction spectra converge to the similar spectrum and peak positions after the growth reaction, which indicates the effect of surface diffusion on determining the

formation of final structure. In addition, we quantitatively analyze the dispersity of Au circular nanoplate growth reaction, as shown in Figure S21. To some extent, there is a dispersity in the plane area of the growth products, which suggest the possibility of heterogeneity in controlled vial synthesis, similar to the LPTEM results. Nevertheless, all of the final structures turn out to be hexagonal nanoplates. We also use different sizes of Au circular nanoplates as a starting material and change the pH or concentration of surfactant during the reformation reaction, all of which leads to hexagonal nanoplate configuration (Figure S22). Overall, the results clearly demonstrate that the surface diffusion of adatoms on the nanocrystal surface plays a key role in determining the final configuration, leading to a universal growth product truncated with stable {111} facets.

## CONCLUSIONS

In conclusion, we directly observe the diverse shape transformations of Au nanocrystals using LPTEM and analyze the transition of individual surface-exposed facets. Oxidative etching of Au nanoprism and reformation of faceted structure are induced by changing the chemical potential in the reaction solution, and observed in LPTEM along with the vial synthesis. Combined with KMC simulations, surface atoms on exposed facets are found to diffuse to unstable {220} facets, resulting in the dominant development of surface-exposed {220} facets into stable {111} facets. The results show that diffusion of surface atoms heavily contribute to the final structure in Au nanocrystal transformation, generating truncated morphology with minimized surface energy. Overall, the surface diffusion, as highlighted in this work, is a critical factor in the shape-controlled synthesis of colloidal nanocrystals.

## METHODS

**Synthesis of Au Nanoprisms.** Triangular Au nanoprisms were synthesized by a three-step seed-mediated method, as reported previously.[40] The first step is to prepare ~5 nm spherical seeds. A total of 20 mM aqueous $HAuCl_4 \cdot 3H_2O$ solution, 1 mL of a 10 mM aqueous solution of sodium citrate, and 1 mL of 100 mM aqueous $NaBH_4$ (ice cold) solution at the last step were added to 36.5 mL of deionized water with a magnetic stirring bar. A mixture of 108 mL of 0.05 M aqueous CTAB solution and 54 $\mu$L of 0.1 M aqueous NaI solution was divided into three containers. Out of this mixture, a total of 9 mL was added to each container labeled 1 and 2. The remaining mixture (90 mL) was transferred to container 3. A mixture of 125 $\mu$L of 20 mM aqueous $HAuCl_4 \cdot 3H_2O$ solution, 50 $\mu$L of 100 mM NaOH, and 50 $\mu$L of 100 mM ascorbic acid (at the last step) was then added to each container 1 and 2. A mixture of 1.25 mL of 20 mM $HAuCl_4 \cdot 3H_2O$ solution, 0.5 mL of 100 mM NaOH, and 0.5 mL of 100 mM ascorbic acid was added to container 3. A total of 1 mL of seed solution was introduced to container 1 with mild shaking, followed by addition of 1 mL of container 1 solution into container 2. After gentle shaking, the entire solution in container 2 was added to container 3.

**Synthesis of Au Circular Nanoplates.** Au circular nanoplates were prepared by oxidative etching process. One mL of 0.1 M HCl and 1 mL of 9% $H_2O_2$ were mixed with 10 mL of Au nanoprisms (OD 1.0 in 785 nm) at 50 °C for 1 h. After 1 h, the extinction band was located to 800 nm. After the etching reaction, the samples were washed twice by centrifugation at 8000 rpm for 20 min.

**Synthesis of Au Hexagonal Nanoplates.** Hexagonal nanoplates were synthesized from Au reduction process. Au circular nanoplates were diluted to 1.0 OD (in 800 nm). A total of 6 mL of circular nanoplates, 1 mL of 0.1 M CTAB, 80 $\mu$L of 0.1 M ascorbic acid, and 20 mM $HAuCl_4$ (at the last step) was added to the 20 mL vial. The reaction was conducted under 30 °C for 6 h. After reaction, the samples were washed twice by centrifugation at 6000 rpm for 20 min.

**In Situ Liquid Phase TEM Investigation.** The flow-type liquid cell (Protochips, USA) consists of bottom chip (550 × 50 $\mu$m window with 150 nm thick spacer) and top chip (550 × 50 $\mu$m window). The thickness of the silicon nitride membrane is 50 nm. A small amount of Au nanoprisms dispersed in deionized water (less than 0.2 $\mu$L) was loaded onto the bottom chip, and the liquid cell was assembled inside the Poseidon select holder (Protochips, USA). For the injection of the etchant solution, mixture of 450 $\mu$L of 1% $H_2O_2$, 450 $\mu$L of 5 mM HCl, and 100 $\mu$L of 1 mM CTAB aqueous solution was loaded into the Hamilton gastight syringe, and injected into the liquid cell through the syringe pump with the flow rate of 120 $\mu$L/h. While such chemical conditions were maintained constantly, the switching from etching to reformation occurred spontaneously as the oxidized Au ions accumulated in the liquid cell. For high oxidizing power to induce oxidative etching of nanoprism exclusively, mixture of 450 $\mu$L of 3% $H_2O_2$, 450 $\mu$L of 10 mM HCl, and 100 $\mu$L of 1 mM CTAB aqueous solution was injected. In a control experiment for studying the effect of different surfactant system on the shape transformation, CTAB was replaced with CTAC. A mixture of 450 $\mu$L of 1% $H_2O_2$, 450 $\mu$L of 5 mM HCl, and 100 $\mu$L of 1 mM CTAC aqueous solution was injected. JEM-2100F TEM (JEOL) was operated for in situ TEM imaging under the acceleration voltage of 200 kV, with an UltraScan 1000XP CCP detector (Gatan). Throughout the in situ imaging, the electron dose rate was maintained to $\sim$ 90 $e^-/Å^2$s, and the movies were recorded in 10 frames per second. It is noteworthy that we used flow-type LPTEM whereby continuous circulation of the fresh solution prohibits accumulation of radiolysis species that might be generated by the e-beam.[65−67] After acquiring in situ movies, we used our homemade MATLAB code to split the movies into time-series images and processed binarization of the TEM images into black and white images for further quantitative analysis.

## ASSOCIATED CONTENT

### ⓢ Supporting Information

The Supporting Information is available free of charge at https://pubs.acs.org/doi/10.1021/acsnano.2c07256.

> Materials, characterization of Au nanocrystals, theoretical model, additional supporting figures and control experiments from LPTEM, KMC, and vial synthesis (PDF)
>
> Videos S1 and S2: In situ LPTEM video showing the oxidative etching of Au nanoprism; scale bars are 100 nm (MP4, MP4)
>
> Videos S3 and S4: In situ LPTEM video showing the oxidative etching of Au nanoprism, followed by a sequential reformation to hexagonal nanoplate; scale bars are 100 nm (MP4, MP4)
>
> Video S5: In situ LPTEM video showing the oxidative etching of Au circular nanoplate, followed by a sequential reformation to hexagonal nanoplate (MP4)
>
> Videos S6 and S7: In situ LPTEM video showing the oxidative etching of Au nanoprism, followed by a sequential reformation when surfactant is exchanged from CTAB to CTAC; scale bars are 100 nm (MP4, MP4)

## AUTHOR INFORMATION

### Corresponding Authors

**Jungwon Park** − *Center for Nanoparticle Research, Institute for Basic Science (IBS), Seoul 08826, Republic of Korea; School of Chemical and Biological Engineering, and Institute of Chemical Process, Seoul National University, Seoul 08826, Republic of Korea; Institute of Engineering Research, College of Engineering, Seoul National University, Seoul 08826, Republic of Korea; Advanced Institutes of Convergence*

*Technology, Seoul National University, Suwon-si, Gyeonggi-do 16229, Republic of Korea;* ⊙ orcid.org/0000-0003-2927-4331; Email: jungwonpark@snu.ac.kr

**Taeghwan Hyeon** − *Center for Nanoparticle Research, Institute for Basic Science (IBS), Seoul 08826, Republic of Korea; School of Chemical and Biological Engineering, and Institute of Chemical Process, Seoul National University, Seoul 08826, Republic of Korea;* ⊙ orcid.org/0000-0001-5959-6257; Email: thyeon@snu.ac.kr

**Shafigh Mehraen** − *Department of Chemical Engineering, University of Illinois at Chicago, Chicago, Illinois 60607, United States;* ⊙ orcid.org/0000-0002-0066-7396; Email: tranzabi@uic.edu

**Sungho Park** − *Department of Chemistry, Sungkyunkwan University, Suwon 16419, Republic of Korea;* ⊙ orcid.org/0000-0001-5435-3125; Email: spark72@skku.edu

### Authors

**Back Kyu Choi** − *Center for Nanoparticle Research, Institute for Basic Science (IBS), Seoul 08826, Republic of Korea; School of Chemical and Biological Engineering, and Institute of Chemical Process, Seoul National University, Seoul 08826, Republic of Korea;* ⊙ orcid.org/0000-0001-8828-2660

**Jeongwon Kim** − *Department of Chemistry, Sungkyunkwan University, Suwon 16419, Republic of Korea;* ⊙ orcid.org/0000-0002-5125-8496

**Zhen Luo** − *Department of Chemical Engineering, University of Illinois at Chicago, Chicago, Illinois 60607, United States*

**Joodeok Kim** − *Center for Nanoparticle Research, Institute for Basic Science (IBS), Seoul 08826, Republic of Korea; School of Chemical and Biological Engineering, and Institute of Chemical Process, Seoul National University, Seoul 08826, Republic of Korea*

**Jeong Hyun Kim** − *Center for Nanoparticle Research, Institute for Basic Science (IBS), Seoul 08826, Republic of Korea; School of Chemical and Biological Engineering, and Institute of Chemical Process, Seoul National University, Seoul 08826, Republic of Korea;* ⊙ orcid.org/0000-0002-9827-8427

Complete contact information is available at:
https://pubs.acs.org/10.1021/acsnano.2c07256

### Notes

The authors declare no competing financial interest.

## REFERENCES

(1) Goesmann, H.; Feldmann, C. Nanoparticulate Functional Materials. *Angew. Chem., Int. Ed.* **2010**, *49*, 1362−1395.

(2) Yoo, S.; Kim, J.; Choi, S.; Park, D.; Park, S. Two-Dimensional Nanoframes with Dual Rims. *Nat. Commun.* **2019**, *10*, 5789.

(3) Jin, R. C.; Zeng, C. J.; Zhou, M.; Chen, Y. X. Atomically Precise Colloidal Metal Nanoclusters and Nanoparticles: Fundamentals and Opportunities. *Chem. Rev.* **2016**, *116*, 10346−10413.

(4) Kwon, S. G.; Hyeon, T. Formation Mechanisms of Uniform Nanocrystals via Hot-Injection and Heat-Up Methods. *Small* **2011**, *7*, 2685−2702.

(5) Xin, H. L. L.; Alayoglu, S.; Tao, R. Z.; Genc, A.; Wang, C. M.; Kovarik, L.; Stach, E. A.; Wang, L. W.; Salmeron, M.; Somorjai, G. A.; Zheng, H. M. Revealing the Atomic Restructuring of Pt-Co Nanoparticles. *Nano Lett.* **2014**, *14*, 3203−3207.

(6) Xia, Y. N.; Xiong, Y. J.; Lim, B.; Skrabalak, S. E. Shape-Controlled Synthesis of Metal Nanocrystals: Simple Chemistry Meets Complex Physics? *Angew. Chem., Int. Ed.* **2009**, *48*, 60−103.

(7) Grzelczak, M.; Perez-Juste, J.; Mulvaney, P.; Liz-Marzan, L. M. Shape Control in Gold Nanoparticle Synthesis. *Chem. Soc. Rev.* **2008**, *37*, 1783−1791.

(8) Mohanty, A.; Garg, N.; Jin, R. C. A Universal Approach to the Synthesis of Noble Metal Nanodendrites and Their Catalytic Properties. *Angew. Chem., Int. Ed.* **2010**, *49*, 4962−4966.

(9) Lai, K. C.; Han, Y.; Spurgeon, P.; Huang, W. Y.; Thiel, P. A.; Liu, D. J.; Evans, J. W. Reshaping, Intermixing, and Coarsening for Metallic Nanocrystals: Nonequilibrium Statistical Mechanical and Coarse-Grained Modeling. *Chem. Rev.* **2019**, *119*, 6670−6768.

(10) Oh, M. H.; Yu, T.; Yu, S. H.; Lim, B.; Ko, K. T.; Willinger, M. G.; Seo, D. H.; Kim, B. H.; Cho, M. G.; Park, J. H.; Kang, K.; Sung, Y. E.; Pinna, N.; Hyeon, T. Galvanic Replacement Reactions in Metal Oxide Nanocrystals. *Science* **2013**, *340*, 964−968.

(11) Xia, Y. N.; Gilroy, K. D.; Peng, H. C.; Xia, X. H. Seed-Mediated Growth of Colloidal Metal Nanocrystals. *Angew. Chem., Int. Ed.* **2017**, *56*, 60−95.

(12) Zhang, T.; Li, X. J.; Li, C. C.; Cai, W. P.; Li, Y. One-Pot Synthesis of Ultrasmooth, Precisely Shaped Gold Nanospheres via Surface Self-Polishing Etching and Regrowth. *Chem. Mater.* **2021**, *33*, 2593−2603.

(13) Kim, B. H.; Heo, J.; Kim, S.; Reboul, C. F.; Chun, H.; Kang, D.; Bae, H.; Hyun, H.; Lim, J.; Lee, H.; Han, B.; Hyeon, T.; Alivisatos, A. P.; Ercius, P.; Elmlund, H.; Park, J. Critical Differences in 3D Atomic Structure of Individual Ligand-Protected Nanocrystals in Solution. *Science* **2020**, *368*, 60−67.

(14) Hauwiller, M. R.; Ye, X. C.; Jones, M. R.; Chan, C. M.; Calvin, J. J.; Crook, M. F.; Zheng, H. M.; Alivisatos, A. P. Tracking the Effects of Ligands on Oxidative Etching of Gold Nanorods in Graphene Liquid Cell Electron Microscopy. *ACS Nano* **2020**, *14*, 10239−10250.

(15) Li, Y. W.; Lin, H. X.; Zhou, W. J.; Sun, L.; Samanta, D.; Mirkin, C. A. Corner-, Edge-, and Facet-Controlled Growth of Nanocrystals. *Sci. Adv.* **2021**, *7*, eabf1410.

(16) Kim, J.; Yoo, S.; Kim, J. M.; Choi, S.; Kim, J.; Park, S. J.; Park, D.; Nam, J. M.; Park, S. Synthesis and Single-Particle Surface-Enhanced Raman Scattering Study of Plasmonic Tripod Nanoframes with Y-Shaped Hot-Zones. *Nano Lett.* **2020**, *20*, 4362−4369.

(17) Straney, P. J.; Andolina, C. M.; Millstone, J. E. Seedless Initiation as an Efficient, Sustainable Route to Anisotropic Gold Nanoparticles. *Langmuir* **2013**, *29*, 4396−4403.

(18) Mayoral, A.; Barron, H.; Estrada-Salas, R.; Vazquez-Duran, A.; Jose-Yacaman, M. Nanoparticle Stability from the Nano to the Meso Interval. *Nanoscale* **2010**, *2*, 335−342.

(19) Drechsler, M.; Blackford, B. L.; Putnam, A. M.; Jericho, M. H. A Measurement of a Surface Self-Diffusion Coefficient by Scanning Tunneling Microscopy. *J. Phys. Colloq.* **1989**, *50*, C8223−C8228.

(20) Dona, J. M.; Gonzalezvelasco, J. The Dependence of the Surface-Diffusion Coefficients of Gold Atoms on the Potential - Its Influence on Reconstruction of Metal Lattices. *Sur. Sci.* **1992**, *274*, 205−214.

(21) Alonso, C.; Salvarezza, R. C.; Vara, J. M.; Arvia, A. J. The Surface-Diffusion of Gold Atoms on Gold Electrodes in Acid-Solution and Its Dependence on the Presence of Foreign Adsorbates. *Electrochim. Acta* **1990**, *35*, 1331−1336.

(22) Boles, M. A.; Ling, D.; Hyeon, T.; Talapin, D. V. The Surface Science of Nanocrystals. *Nat. Mater.* **2016**, *15*, 141−153.

(23) Yang, T. H.; Shi, Y. F.; Janssen, A.; Xia, Y. N. Surface Capping Agents and Their Roles in Shape-Controlled Synthesis of Colloidal Metal Nanocrystals. *Angew. Chem., Int. Ed.* **2020**, *59*, 15378−15401.

(24) Zherebetskyy, D.; Scheele, M.; Zhang, Y. J.; Bronstein, N.; Thompson, C.; Britt, D.; Salmeron, M.; Alivisatos, P.; Wang, L. W. Hydroxylation of the Surface of PbS Nanocrystals Passivated with Oleic Acid. *Science* **2014**, *344*, 1380−1384.

(25) Ghosh, S.; Manna, L. The Many "Facets" of Halide Ions in the Chemistry of Colloidal Inorganic Nanocrystals. *Chem. Rev.* **2018**, *118*, 7804−7864.

(26) Negishi, Y.; Nakazaki, T.; Malola, S.; Takano, S.; Niihori, Y.; Kurashige, W.; Yamazoe, S.; Tsukuda, T.; Hakkinen, H. A Critical Size for Emergence of Nonbulk Electronic and Geometric Structures in Dodecanethiolate-Protected Au Clusters. *J. Am. Chem. Soc.* **2015**, *137*, 1206−1212.

(27) Eustis, S.; El-Sayed, M. A. Why Gold Nanoparticles are More Precious than Pretty Gold: Noble Metal Surface Plasmon Resonance and Its Enhancement of the Radiative and Nonradiative Properties of Nanocrystals of Different Shapes. *Chem. Soc. Rev.* **2006**, *35*, 209−217.

(28) Wiley, B. J.; Chen, Y. C.; McLellan, J. M.; Xiong, Y. J.; Li, Z. Y.; Ginger, D.; Xia, Y. N. Synthesis and Optical Properties of Silver Nanobars and Nanorice. *Nano Lett.* **2007**, *7*, 1032−1036.

(29) Loh, N. D.; Sen, S.; Bosman, M.; Tan, S. F.; Zhong, J.; Nijhuis, C. A.; Kral, P.; Matsudaira, P.; Mirsaidov, U. Multistep Nucleation of Nanocrystals in Aqueous Solution. *Nat. Chem.* **2017**, *9*, 77−82.

(30) Kim, B. H.; Yang, J.; Lee, D.; Choi, B. K.; Hyeon, T.; Park, J. Liquid-Phase Transmission Electron Microscopy for Studying Colloidal Inorganic Nanoparticles. *Adv. Mater.* **2018**, *30*, 1703316.

(31) Ou, Z. H.; Wang, Z. W.; Luo, B. B.; Luijten, E.; Chen, Q. Kinetic Pathways of Crystallization at the Nanoscale. *Nat. Mater.* **2020**, *19*, 450−455.

(32) Ye, X. C.; Jones, M. R.; Frechette, L. B.; Chen, Q.; Powers, A. S.; Ercius, P.; Dunn, G.; Rotskoff, G. M.; Nguyen, S. C.; Adiga, V. P.; Zettl, A.; Rabani, E.; Geissler, P. L.; Alivisatos, A. P. Single-Particle Mapping of Nonequilibrium Nanocrystal Transformations. *Science* **2016**, *354*, 874−877.

(33) Chee, S. W.; Tan, S. F.; Baraissov, Z.; Bosman, M.; Mirsaidov, U. Direct Observation of the Nanoscale Kirkendall Effect During Galvanic Replacement Reactions. *Nat. Commun.* **2017**, *8*, 1224.

(34) Jin, B.; Wang, H. F.; Sushko, M. L.; Jin, C. H.; Tang, R. K. The Formation and Shape Transformation Mechanism of a Triangular Au Nanoplate Revealed by Liquid-Cell TEM. *Nanoscale* **2020**, *12*, 19592−19596.

(35) Wu, J. B.; Gao, W. P.; Yang, H.; Zuo, J. M. Dissolution Kinetics of Oxidative Etching of Cubic and Icosahedral Platinum Nanoparticles Revealed by in Situ Liquid Transmission Electron Microscopy. *ACS Nano* **2017**, *11*, 1696−1703.

(36) Alloyeau, D.; Dachraoui, W.; Javed, Y.; Belkahla, H.; Wang, G.; Lecoq, H.; Ammar, S.; Ersen, O.; Wisnet, A.; Gazeau, F.; Ricolleau, C. Unravelling Kinetic and Thermodynamic Effects on the Growth of Gold Nanoplates by Liquid Transmission Electron Microscopy. *Nano Lett.* **2015**, *15*, 2574−2581.

(37) Ma, X. M.; Lin, F.; Chen, X.; Jin, C. H. Unveiling Growth Pathways of Multiply Twinned Gold Nanoparticles by in Situ Liquid Cell Transmission Electron Microscopy. *ACS Nano* **2020**, *14*, 9594−9604.

(38) Son, Y.; Kim, B. H.; Choi, B. K.; Luo, Z.; Kim, J.; Kim, G. H.; Park, S. J.; Hyeon, T.; Mehraeen, S.; Park, J. In Situ Liquid Phase TEM of Nanoparticle Formation and Diffusion in a Phase-Separated Medium. *ACS Appl. Mater. Interfaces* **2022**, *14*, 22810−22817.

(39) Park, J. H.; Schneider, N. M.; Grogan, J. M.; Reuter, M. C.; Bau, H. H.; Kodambaka, S.; Ross, F. M. Control of Electron Beam-Induced Au Nanocrystal Growth Kinetics through Solution Chemistry. *Nano Lett.* **2015**, *15*, 5314−5320.

(40) Millstone, J. E.; Park, S.; Shuford, K. L.; Qin, L. D.; Schatz, G. C.; Mirkin, C. A. Observation of a Quadrupole Plasmon Mode for a Colloidal Solution of Gold Nanoprisms. *J. Am. Chem. Soc.* **2005**, *127*, 5312−5313.

(41) Lofton, C.; Sigmund, W. Mechanisms Controlling Crystal Habits of Gold and Silver Colloids. *Adv. Funct. Mater.* **2005**, *15*, 1197−1208.

(42) Kirkland, A. I.; Jefferson, D. A.; Duff, D. G.; Edwards, P. P.; Gameson, I.; Johnson, B. F. G.; Smith, D. J. Structural Studies of Trigonal Lamellar Particles of Gold and Silver. *P. R. Soc. London a-Mater.* **1993**, *440*, 589−609.

(43) Hong, S.; Shuford, K. L.; Park, S. Shape Transformation of Gold Nanoplates and their Surface Plasmon Characterization: Triangular to Hexagonal Nanoplates. *Chem. Mater.* **2011**, *23*, 2011−2013.

(44) Germain, V.; Li, J.; Ingert, D.; Wang, Z. L.; Pileni, M. P. Stacking Faults in Formation of Silver Nanodisks. *J. Phys. Chem. B* **2003**, *107*, 8717−8720.

(45) Hauwiller, M. R.; Ondry, J. C.; Chan, C. M.; Khandekar, P.; Yu, J.; Alivisatos, A. P. Gold Nanocrystal Etching as a Means of Probing the Dynamic Chemical Environment in Graphene Liquid Cell Electron Microscopy. *J. Am. Chem. Soc.* **2019**, *141*, 4428−4437.

(46) Long, R.; Zhou, S.; Wiley, B. J.; Xiong, Y. J. Oxidative Etching for Controlled Synthesis of Metal Nanocrystals: Atomic Addition and Subtraction. *Chem. Soc. Rev.* **2014**, *43*, 6288−6310.

(47) Zhu, Q.; Wu, J.; Zhao, J.; Ni, W. Role of Bromide in Hydrogen Peroxide Oxidation of CTAB-Stabilized Gold Nanorods in Aqueous Solutions. *Langmuir* **2015**, *31*, 4072−4077.

(48) da Silva, J. A.; Netz, P. A.; Meneghetti, M. R. Growth Mechanism of Gold Nanorods: the Effect of Tip-Surface Curvature as Revealed by Molecular Dynamics Simulations. *Langmuir* **2020**, *36*, 257−263.

(49) Ni, W. H.; Kou, X.; Yang, Z.; Wang, J. F. Tailoring Longitudinal Surface Plasmon Wavelengths, Scattering and Absorption Cross Sections of Gold Nanorods. *ACS Nano* **2008**, *2*, 677−686.

(50) Deng, T. S.; van der Hoeven, J. E. S.; Yalcin, A. O.; Zandbergen, H. W.; van Huis, M. A.; van Blaaderen, A. Oxidative Etching and Metal Overgrowth of Gold Nanorods within Mesoporous Silica Shells. *Chem. Mater.* **2015**, *27*, 7196−7203.

(51) Janicek, B. E.; Hinman, J. G.; Hinman, J. J.; Bae, S. H.; Wu, M.; Turner, J.; Chang, H. H.; Park, E.; Lawless, R.; Suslick, K. S.; Murphy, C. J.; Huang, P. Y. Quantitative Imaging of Organic Ligand Density on Anisotropic Inorganic Nanocrystals. *Nano Lett.* **2019**, *19*, 6308−6314.

(52) González-Velasco, J.; Doña, J. M. Mechanism of Surface Diffusion of Gold Adatoms in Contact with an Electrolytic Solution. *J. Phys. Chem.* **1993**, *97*, 4714−4719.

(53) McCue, I.; Benn, E.; Gaskey, B.; Erlebacher, J. Dealloying and Dealloyed Materials. *Annu. Rev. Mater. Res.* **2016**, *46*, 263−286.

(54) Alonso, C.; Salvarezza, R. C.; Vara, J. M.; Arvia, A. J.; Vazquez, L.; Bartolome, A.; Baro, A. M. The Evaluation of Surface Diffusion Coefficients of Gold and Platinum Atoms at Electrochemical Interfaces from Combined STM-SEM Imaging and Electrochemical Techniques. *J. Electrochem. Soc.* **1990**, *137*, 2161−2166.

(55) Sieradzki, K. Curvature Effects in Alloy Dissolution. *J. Electrochem. Soc.* **1993**, *140*, 2868−2872.

(56) Li, X.; Chen, Q.; McCue, I.; Snyder, J.; Crozier, P.; Erlebacher, J.; Sieradzki, K. Dealloying of Noble-Metal Alloy Nanoparticles. *Nano Lett.* **2014**, *14*, 2569−2577.

(57) Chandler, D. *Introduction to Modern Statistical Mechanics*, 1st; Oxford University Press: New York, 1987; pp 124−131.

(58) Schneider, N. M.; Norton, M. M.; Mendel, B. J.; Grogan, J. M.; Ross, F. M.; Bau, H. H. Electron-Water Interactions and Implications for Liquid Cell Electron Microscopy. *J. Phys. Chem. C* **2014**, *118*, 22373−22382.

(59) Meena, S. K.; Celiksoy, S.; Schafer, P.; Henkel, A.; Sonnichsen, C.; Sulpizi, M. The Role of Halide Ions in the Anisotropic Growth of

Gold Nanoparticles: a Microscopic. *Atomistic Perspective. Phys. Chem. Chem. Phys.* **2016**, *18*, 13246−13254.

(60) Thanh, N. T. K.; Maclean, N.; Mahiddine, S. Mechanisms of Nucleation and Growth of Nanoparticles in Solution. *Chem. Rev.* **2014**, *114*, 7610−7630.

(61) Singh-Miller, N. E.; Marzari, N. Surface Energies, Work Functions, and Surface Relaxations of Low-Index Metallic Surfaces from First Principles. *Phys. Rev. B* **2009**, *80*, No. 235407.

(62) Vitos, L.; Ruban, A. V.; Skriver, H. L.; Kollar, J. The Surface Energy of Metals. *Surf. Sci.* **1998**, *411*, 186−202.

(63) Ding, Y.; Kim, Y.; Erlebacher, J. Nanoporous Gold Leaf: "Ancient Technology"/Advanced Material. *Adv. Mater.* **2004**, *16*, 1897−1900.

(64) Almora-Barrios, N.; Novell-Leruth, G.; Whiting, P.; Liz-Marzan, L. M.; Lopez, N. Theoretical Description of the Role of Halides, Silver, and Surfactants on the Structure of Gold Nanorods. *Nano Lett.* **2014**, *14*, 871−875.

(65) Egerton, R. F.; Li, P.; Malac, M. Radiation Damage in the TEM and SEM. *Micron* **2004**, *35*, 399−409.

(66) Chen, Q.; Dwyer, C.; Sheng, G.; Zhu, C.; Li, X.; Zheng, C.; Zhu, Y. Imaging Beam-Sensitive Materials by Electron Microscopy. *Adv. Mater.* **2020**, *32*, 1907619.

(67) Ou, Z.; Liu, C.; Yao, L.; Chen, Q. Nanoscale Cinematography of Soft Matter System under Liquid-Phase TEM. *Acc. Mater. Res.* **2020**, *1*, 41−52.